Available online at www.sciencedirect.com

ScienceDirect

International Journal of Multiphase Flow 33 (2007) 147–163

International Journal of Multiphase Flow

www.elsevier.com/locate/ijmulflow

Skin friction reduction by large air bubbles in a horizontal channel flow

Yuichi Murai [a,*], Hiroshi Fukuda [b], Yoshihiko Oishi [a],
Yoshiaki Kodama [c], Fujio Yamamoto [b]

[a] *Division of Energy & Environmental System, Graduate School of Engineering, Hokkaido University, Kita-ku, N13W8, Sapporo, 060-8628, Japan*
[b] *Division of Fiber Amenity Engineering, Graduate School of Engineering, University of Fukui, Bunkyo 3-9-1, Fukui, 910-8507, Japan*
[c] *National Maritime Research Institute of Japan, Shinkawa 6-38-1, Mitaka, Tokyo, 181-0004, Japan*

Received 17 October 2005; received in revised form 15 August 2006

Abstract

Microbubble and air film methods are believed to be applicable to skin friction reduction in ships. Small bubbles are dispersed into the turbulent boundary layer in the former case, and wide air layers cover the wall surface in the latter case. Previous studies did not specifically address the intermediate case between the microbubble and air film conditions. This study is concerned with the possibility and mechanism of drag reduction using relatively large air bubbles compared to the boundary layer thickness in a horizontal turbulent channel flow. The relationship between local skin friction and the bubble's interfacial structure is investigated by synchronizing the measurement of wall-shear stress with the image acquisition of bubbles. The bubble sizes range from 2 to 90 mm approximately. As a result, a negative correlation between the local skin friction and the local void fraction is confirmed by the time-resolved measurement. A new observation is the fact that the local skin friction decreases drastically in the rear part of individual large bubbles, and rapidly increases after the bubble's rear interface passes. This characteristic underlies the bubble-size dependency of the average skin friction in the intermediate bubble size condition.

Keywords: Drag reduction; Bubble dynamics; Turbulent flow; Skin friction; Air film

---

1. Introduction

Various methods for reducing skin frictional drag in turbulent flows have been proposed in the past. One such method – the use of bubbles – has recently become a focus for engineers in the expectation that it might be applicable to ships and pipelines. There are two main approaches to the utilisation of bubbles, depending

---

[*] Corresponding author. Tel.: +81 11 706 6372; fax: +81 11 706 7889.
E-mail address: murai@eng.hokudai.ac.jp (Y. Murai).

0301-9322/$ - see front matter © 2006 Elsevier Ltd. All rights reserved.
doi:10.1016/j.ijmultiphaseflow.2006.08.008

upon the bubbles' size. One is the so-called 'microbubble' method, first reported by McCormick and Bhattacharyya (1973). They employed electrolysis to generate microbubbles in water and were able to demonstrate some degree of drag reduction for a submersible hull. Laboratory experiments using a water tunnel or channel have also been carried out in a number of hydrodynamic research institutes in order to characterize the skin friction reduction process associated with small bubbles and to determine the parameters involved (Madavan et al., 1985; Merkle and Deutsch, 1992; Kato et al., 1999; Kodama et al., 2000; Moriguchi and Kato, 2002; Gabillet et al., 2002). Several theoretical discussions have been published by Legner (1984) and Marie (1987) to try to explain the drag reduction mechanism simply, by reference to such aspects as the reduction in density of the mixture and modification of the effective viscosity inside the boundary layer. In parallel, numerical researches mainly dealing with small spherical bubbles were reported by Felton and Loth (2002), Xu et al. (2002) and Ferrante and Elghobashi (2004), to elaborate on the drag reduction process. Tests of the application of small bubbles to ships or long flat plates were reported by Takahashi et al. (2003) and Latorre et al. (2003). Some of the above experiments involved relatively large bubbles compared to the boundary layer thickness. However, these authors often still use the term "microbubbles" in a qualitative sense, because the bubble size is undoubtedly smaller than the effective length of the drag-reducing area. After considering many sets of published experimental data, we can say that not only "real microbubbles" but also "a-few-millimeter bubbles" can reduce skin friction, as reported by Moriguchi and Kato (2002). They found that there appears to be no significant bubble size dependency in conditions of high shear rate. Therefore, recent discussion has moved on to the role of the bubble's deformability in helping to reduce the local Reynolds shear stress, as reported by Kitagawa et al. (2005) and Murai et al. (2006). In this context, the bubble is not required to be so small in size or Weber number. In other words, a mechanism of drag reduction independent of that involving spherical bubbles may take place after the bubbles start to deform.

An alternative technique for drag reduction is the 'air film' method, which has been the subject of attempts to make it practicable for the last two decades (e.g. Katsui et al., 2003). The air film method simply cuts off contact between the water and the wall surface. Therefore, the technical problem is just how to maintain a stable air sheet on the target wall. The introduction of a water-repellent surface is examined by Fukuda et al. (2000) and Matsumura et al. (2002). Unfortunately, the air film easily breaks up to become large bubbles downstream, owing to Kelvin–Helmholtz instability. When streamwise persistency of drag reduction is desired, the bubble size after collapse is very important in determining the total drag reduction. If the bubble size is still large enough, the drag reduction should be maintained to some extent. If the size is in a particular range relative to the boundary layer thickness, the drag would increase, owing to enhanced turbulent momentum transfer by the bubbles. However, the critical bubble size, at which drag reduction due to the air film principle disappears, has not been investigated hitherto.

In fact, the above-mentioned two approaches to the utilisation of bubbles, i.e., the microbubble method and the air film method, have been investigated separately. Furthermore, their performance has not been investigated specifically in the intermediate condition between the microbubble and air film methods, i.e. across a range of bubble diameters relative to the thickness of the boundary layer. Furthermore, in the microbubble method, bubbles that are a few millimetres in diameter frequently coalesce in the shear layer and become large bubbles in the downstream region. Therefore, it is important to study this range of bubble sizes and to investigate the persistency of drag reduction along the streamwise length. In our experiments, direct measurement of time averaged skin friction in a horizontal channel is made in conditions intermediate between those of the microbubble and air film approaches. Simultaneously the temporal relationship between local skin friction and bubble interfacial structure is investigated via a synchronized measurement system. This synchronized measurement provided a new understanding of bubble-induced drag reduction, which is explained in detail in this paper.

2. Experimental method

2.1. Experimental apparatus

A schematic diagram of the experimental apparatus is as shown in Fig. 1. The test section is a horizontal rectangular channel made of transparent acrylic resin, 10 mm in height, 100 mm in width and 6000 mm in

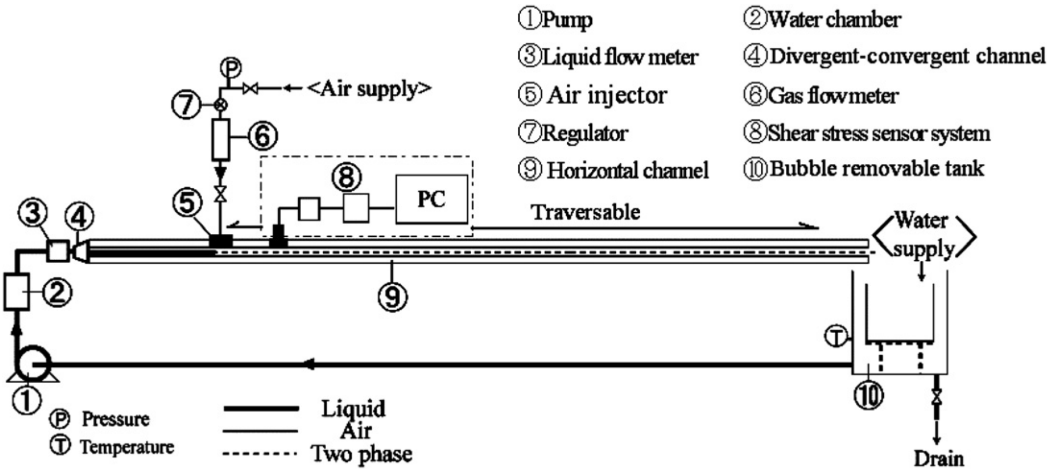

Fig. 1. Experimental apparatus.

length. The two-phases used are tap water and room air at a laboratory temperature of around 28 °C. Air bubbles are injected into the horizontal channel through an air injection device, as shown in Fig. 2. This device has a porous plate made of alumina with a nominal pore diameter of approximately 60 μm and an injection area of $14 \times 48\ \text{mm}^2$. The bubbles are generated with compressed air supplied from outside the channel. The water circulates in the channel, and the bubbles are eliminated in the downstream region by swirling the fluid in a bubble removal tank. The mean liquid velocity in the channel is between 1 and 2 m/s. It is worth noting that the present combination of fluids corresponds to contaminated situation from the viewpoint of bubble dynamics. That is, the gas–liquid interface has different properties from completely clean situation owing to molecular impurity that provides a surfactant effect. In addition, it is well known that additive of surfactant in water reduces mean bubble diameter (Winkel et al., 2004), by which a wide range in bubble size can be examined. The present study, however, aims on large bubbles of Weber number higher than 70, of which behavior is almost independent on such a modification of the interfacial properties. What we investigate here is the performance of frictional drag reduction provided by large bubbles.

2.2. Direct measurement of skin friction

The local wall-shear stress on the upper wall of the channel is measured by a shear transducer (SSK, S10W-01) the set-up for which is illustrated in Fig. 3. The sensor of the shear transducer is 10 mm in diameter and has a maximum measurable load of 1 mN, corresponding to 12.5 Pa of shear stress. The flatness of the sensing area relative to the inner wall surface of the channel is carefully controlled using a gauge plate. There is a

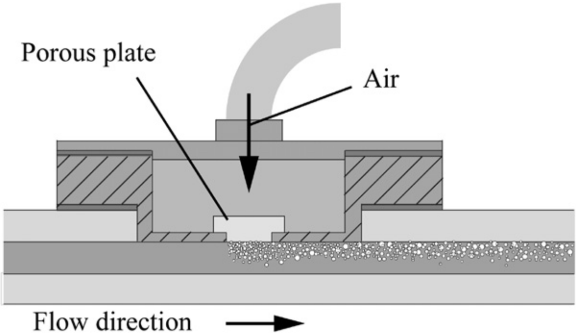

Fig. 2. Air injection device with a porous plate.

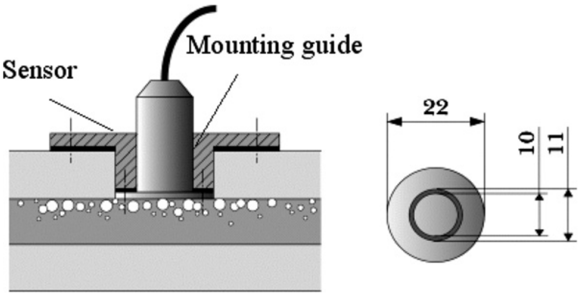

Fig. 3. Schematic diagram of shear transducer. (a) And (b) show the diagram of installing the shear transducer in the channel and the size of sensing area of the shear transducer. The flatness of the sensing area relative to the channel wall is tuned carefully.

gap of 0.5 mm between the sensing disk and the flange, which corresponds to 150–300 wall units for the bulk mean velocity $U = 1–2$ m/s. These two factors, i.e. the flatness error and the gap structure, are un-ignorable factors causing a bias error that is mentioned in Section 2.5. The voltage signal of the shear transducer is imported to a PC through an amplifier and data logger. The measurement locations are set at $x/H = 25$, 100 and 400, which correspond to 250, 1000 and 4000 mm downstream of the air injection device. Details of the experimental conditions are summarised in Table 1.

2.3. Definition of skin friction coefficient

The skin friction coefficient C_f is defined by the following equation:

$$C_f = \frac{\tau_w}{\rho U^2/2} \tag{1}$$

where τ_w is the local wall-shear stress measured by the shear transducer, ρ the density of liquid, and U the bulk mean velocity in the channel. The modification of C_f is studied when the bulk mean velocity U and the void fraction α changes. These two control parameters are given by,

$$\alpha = \frac{Q_a}{Q_w + Q_a} \tag{2}$$

$$U = \frac{Q_w + Q_a}{HB} \tag{3}$$

where H (=2h) is the channel height and B the channel width. The subscripts a and w indicate air and water phases, respectively. The flow rates of two-phases are measured independently by respective flow meters. In the experimentation, U increases due to the volumetric increase in the flow as the air bubbles are injected into

Table 1
Experimental conditions

Bulk mean velocity, U	1.0–2.0 m/s
Mean void fraction, α	0–26%
$Re = UH/\nu$, $H = 2h$	12,000–17,000
$Re_\tau = U_f h/\nu$	340–610
$Fr = U(gh)^{1/2}$	4.5–9.0
$We = \rho_l U^2 h/\sigma$	70–285
Temperature of water	28 °C
Density of water, ρ	999 kg/m^3
Kinematic viscosity, ν	1.17×10^{-6} m^2/s
Shear transducer:	
Sampling rate	1 kHz
Sampling time	60 s

the channel. This acceleration effect leads to superficial increment of the skin friction, and must be eliminated to focus on the bubble's effect on the skin friction. Therefore, the skin friction coefficient of single-phase flow C_{f0} is corrected by the following equation (Kodama et al., 2000) to adjust the same bulk mean velocity.

$$C_{f0} = C_{f0}|_{U_0} \times \frac{\tau_{wU}}{\tau_{wU_0}} \tag{4}$$

where, τ_{wU} is the wall-shear stress estimated by the Blasius formula, and the subscript 0 indicates the bubble-free condition. In this study, the skin friction ratio, i.e. the ratio of skin friction coefficient with bubbles to that without bubbles, is employed to evaluate the modification of the drag.

It is noted that the bubbles in the present channel distribute actually to the top half of the channel due to buoyancy. Thus the modification of skin friction on the upper wall is substantially caused by near-wall void fraction rather than by the bulk void fraction. The ratio of the near-wall to the bulk void fraction ranges from 2 to 5 dependent on the bubble size and the flow speed. The velocity profile in the case of bubbling condition also becomes asymmetric in the vertical direction. Such an asymmetric structure is, however, positioned as experimental result but not a control parameter. An alternative void fraction that actually works for the skin friction reduction will be introduced in the section of discussion.

2.4. Synchronized measurement system

Photography of the interfacial structure of the bubbles is achieved using a high-speed digital video camera (Photron, FASTCAM-MAX), on which a telecentric lens is mounted. Backlight projection is employed to capture the bubble interfaces as shadows, using a metal halide lamp. The frame rate is 500 fps and the shutter speed is 1/150,000 s. The images taken by the camera are recorded as digital raw image data into a PC. The field of view is 17.5 mm × 17.5 mm and the spatial resolution is 0.00172 mm/pixel.

Fig. 4 shows a schematic diagram of the synchronized measurement system. A pulse generator synchronizes the trigger timings of the camera and the data logger. The image acquisition position is 55 mm downstream from the measurement position for wall-shear stress, because they cannot be physically located in the same place. Hence there is a time lag between the data obtained from the two devices. This time lag is removed in the process of data correction using the local mean advection velocity of the bubble interface, which is measured by particle image velocimetry (PIV). The advection velocity of the bubble has a relative velocity to the mean velocity in the channel, as will be described later.

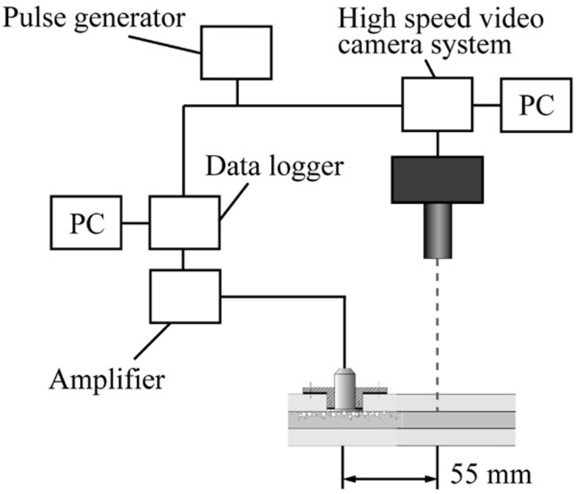

Fig. 4. Sketch of synchronized measurement system.

2.5. Measurement uncertainty of the shear transducer

Fig. 5 shows the results for wall shear stress obtained by the shear transducer in the case of single-phase water channel flow. The theoretical values of Blasius and Plantdl's formulae are shown too, as reference. The velocity information required to calculate the formulae is given by measured flow rate and the assumption of fully developed turbulent flow. As seen in the figure, there is a slight difference between the experimental values and the theoretical values. This discrepancy comes from a very small error in the flatness of the sensing area relative to the channel wall, which is of the order of 10 μm estimated by boundary layer theory. Further reduction of the flatness error was not achieved in this study, since the error displacement is already restricted to within 10^{-3} to the length scale of the sensing area. However the overall trend in both sets of data remains similar, and there is only a bias error relative to Blasius's formula of around −10% in the range tested. This bias error is removed when the absolute value of the skin friction is assessed. For the ratio of the skin friction to that of single-phase condition, C_f/C_{f0}, the bias error unmodifies the resultant value.

Fig. 6 shows a power spectrum of the wall shear stress measured by the present shear transducer. The time serial signal of the transducer is transferred to a data logger at 1 kHz in sampling frequency. The nominal frequency response of the transducer is 20 Hz. The actual natural frequency is assessed by the spectral analysis

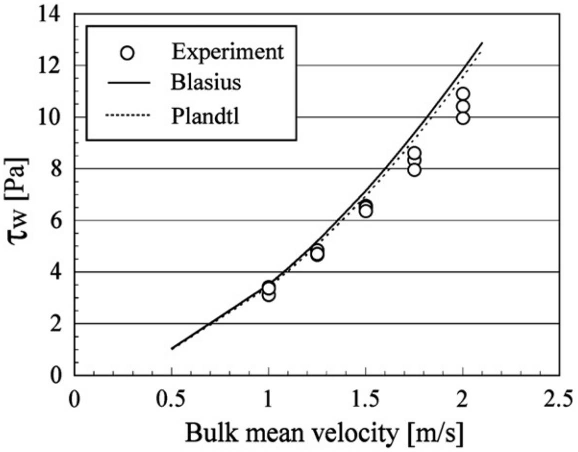

Fig. 5. Wall-shear stress vs. bulk mean velocity at $x/H = 25$, 100 and 400. The solid and broken lines indicate the theoretical values calculated by using Blasius and Plandtle formulae.

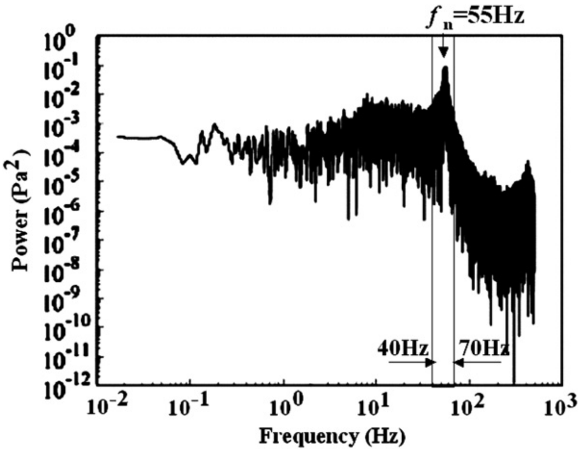

Fig. 6. Power spectrum of shear transducer for single-phase flow at $x/H = 400$, $U = 1.0$ m/s. Natural frequency is obtained as $f_n = 55$ Hz, and the frequency component for $40 < f < 70$ Hz is removed from the wave using a notch filter.

and is obtained as $f_n = 55$ Hz as shown in the figure. The power on it has more than 100 times as neighbor frequency, and its band is fixed narrowly. Therefore, a notch filter, i.e. reversed band-pass filter, is applied to remove only the resonance component from the wave data. The filtering band is from 40 to 70 Hz. The correlation of the instantaneous shear stress to individual bubble passage is investigated by the full range of the sampling frequency of the data logger. Thus the effective temporal resolution is 0.025 s, which is smaller than the typical period of a bubble to spend for passing the sensor.

3. Measurement results and discussion

3.1. Average skin friction vs. bulk void fraction

Fig. 7 shows the results for skin friction on the upper wall at $x/H = 25$, 100 and 400, i.e. $x = 250$, 1000 and 4000 mm downstream from the air injection device. At the position of $x/H = 25$ (see Fig. 7a), the skin friction

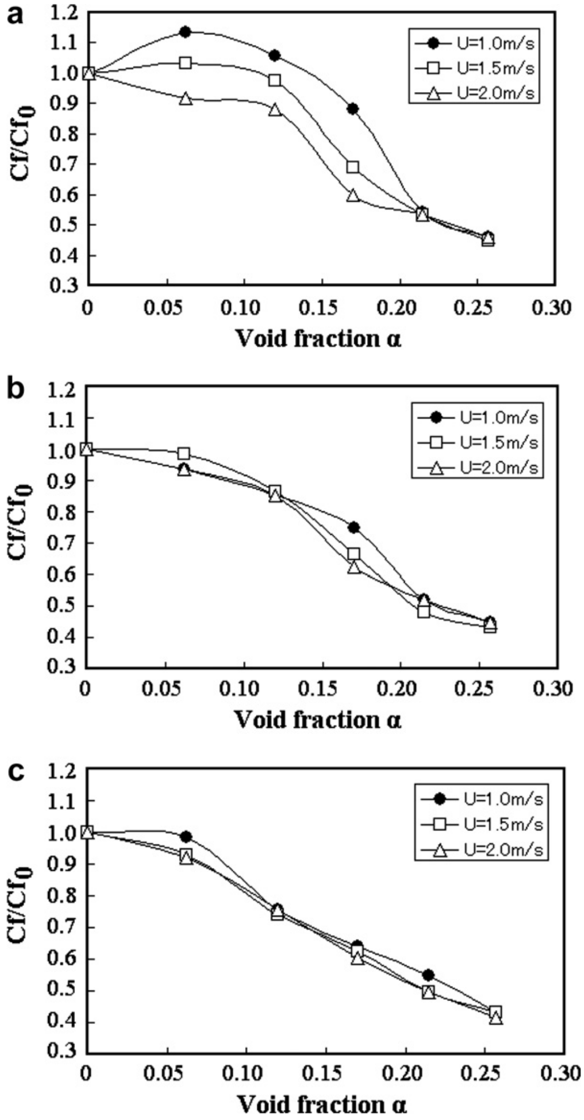

Fig. 7. The skin friction ratio vs. void fraction. (a–c) Show the case of $x/H = 25$, 100 and 400. The symbols indicate the case of bulk mean velocity in the channel.

ratio increases with increasing void fraction up to around 10%. And then it begins to decrease at higher void fractions. The skin friction ratio becomes lower than unity once the void fraction becomes higher than 15%. That is, drag reduction occurs in the presence of bubbles. The maximum drag reduction observed in the present experiment is 55% by supplying a void fraction of 26%. It is also seen that variation in the data owing to the speed of flow is obvious at the lower void fraction. The skin friction ratio decreases as the flow velocity increases. This trend of the flow speed dependence appears because of two factors. One is bubble size changing significantly with the flow speed, as mentioned later. Another is transient effect of the boundary layer development as a bubbly two-phase flow. In contrast, this deviation vanishes once the void fraction achieves higher than 20%. This supports the basic idea that drag reduction results simply from the air-covered area in the case of enough large bubbles.

With regard to the different measurement points, the skin friction ratio is always lower than unity at $x/H = 100$ and 400 (see Fig. 7b and c). The skin friction at such downstream locations decreases approximately linearly as void fraction increases. When the void fraction is higher than 20%, it is found that the skin friction ratio approaches a steady value at all flow velocities and measurement positions. This result implies conversely that at $x/H = 25$ there is a transient effect of a two-phase boundary layer developing in the streamwise direction. The distance that this transient effect extends depends on the speed of channel flow. The two-phase boundary reaches an equilibrium state in the downstream region, which is almost independent of the speed of the flow. We have also measured the pressure drop using two pressure transducers located at $x/H = 25$ and $x/H = 50$. The measured pressure drop normalized in the same way as Eq. (4) was constant independently both on the void fraction and the speed of the flow. This indicates that while the upper wall reduces the skin friction with bubbles, the lower wall receives additional friction of the same amount. Thus the alternation of the channel flow happens only near the upper wall but does not modify the global energy dissipation.

A gain factor of skin friction reduction to void fraction is calculated and shown in Fig. 8. The gain factor is defined by the following equation, which evaluates the drag reduction relative to density reduction of two-phase mixture.

$$G = \frac{1}{\alpha}\left(1 - \frac{C_{\mathrm{f}}}{C_{\mathrm{f0}}}\right) \tag{5}$$

When drag reduction occurs, the gain factor takes a positive value. When the gain factor exceeds unity, it indicates that the drag reduction is promoted more than bulk density reduction of mixture. It realizes so if bubbles are accumulated in the upper wall. The result shows that the gain factor increases with increasing void fraction in all the conditions tested. As the void fraction is supplied higher than 20%, the gain factor grows up and converges to approximately 2 regardless the position x/H and the flow speed U. This convergence explains that the drag reduction is realized simply by cut-off of the liquid contact with the wall when sufficiently large

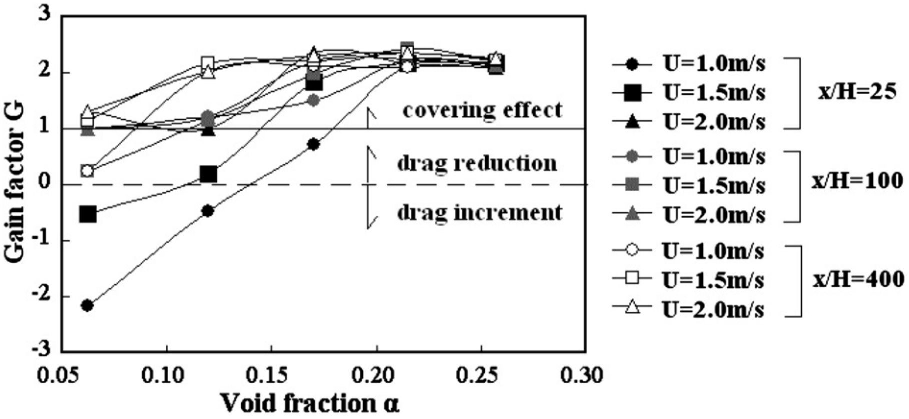

Fig. 8. Gain factor of skin friction reduction to void fraction.

amount of bubbles are mixed. To the contrary, it depends on x/H and U for insufficient void fraction, and generally takes the value smaller than unity. More detailed measurement to elucidate such a parametric dependence will be discussed in Sections 3.3 and 3.4.

3.2. Image measurement of bubbles

The typical bubble shape in the channel is shown in Fig. 9. The upper and lower figures show the images taken from the top and the side of the channel, respectively, using the backlight method. The flow direction is from left to right. In these pictures, the individual bubble is seen to have a non-spherical shape involving a capillary wave in the rear part. The capillary wave observed here is a steady wave, which moves together with the bubble. This wave is induced by a strong curvature of the bubble interface at the rear part where liquid pushes the bubbles.

Fig. 10 shows the relationship between the mean bubble diameter and the bulk mean void fraction. The bubble diameter is measured by analysing the area of an individual bubble image taken from the top. Thus the diameter here is defined by two-dimensional circle-equilibrium diameter. From this figure, it is confirmed that the bubble diameter becomes larger with increasing bulk mean void fraction and distance from the air injection device. Considering the data with the drag reduction performance shown by Figs. 7 and 8, the present skin friction drag reduction occurs with larger bubbles in the case of the higher void fractions, as mentioned next.

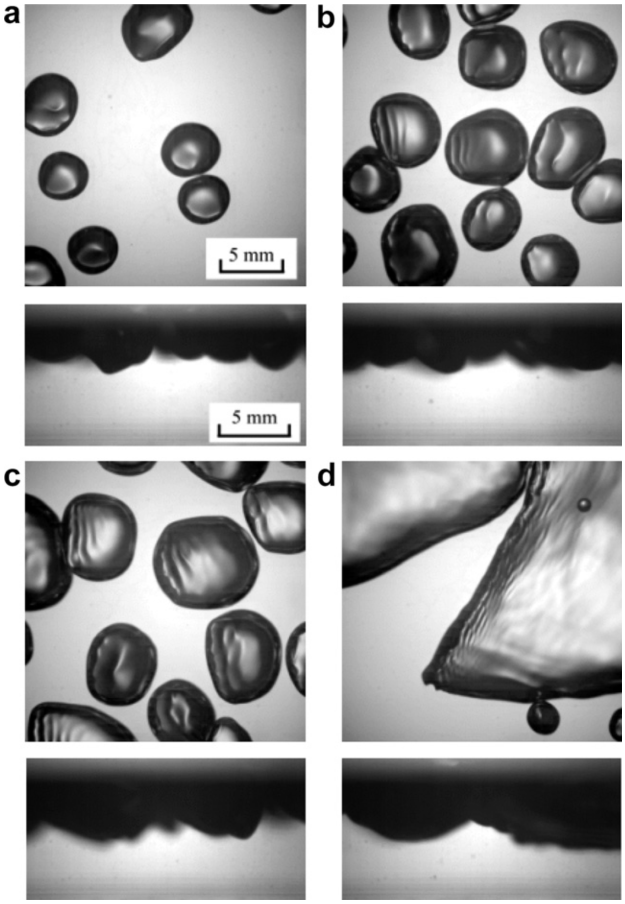

Fig. 9. Snap shots of bubbles in the channel (top and side views at $x/H = 25$, $U = 1.0$ m/s): (a) void fraction of 4.0%; (b) 7.7%; (c) 14.3%; (d) 20.0%.

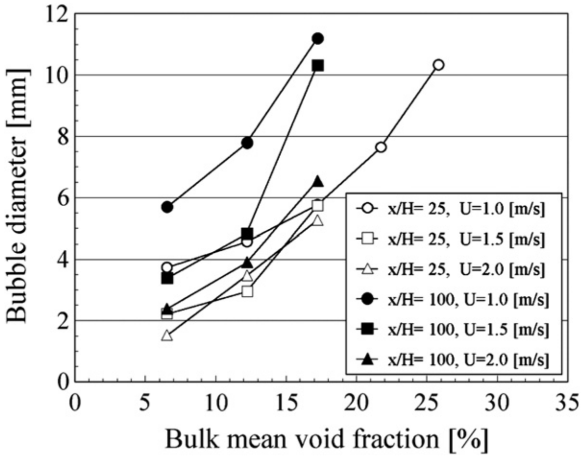

Fig. 10. Void fraction vs. bubble diameter in the conditions of $U = 1.0$, 1.5, 2.0 m/s and $x/H = 25$, 100.

Fig. 11 shows the relationship between mean bubble diameter and skin friction, where the dimensionless bubble diameter d^* is scaled by the half-height of the channel $H/2$. The skin friction reaches its maximum value at $d^* \sim 1$ and tends to decrease from it by increasing d^* or decreasing d^*. This result indicates that either smaller or larger bubbles are required to provide drag reduction, and we need to avoid the intermediate bubble size of around $d^* = 1$. The reason of the bubble size dependency is explained by the alternation of flow field around a single bubble. For a bubble of $d^* > 1$, wall-covering effect of bubbles reduces the contact friction of liquid. Namely, the drag reduction is obtained with structural alternation of the boundary layer to local stratified two-phase flow. This can be, in other words, a one-dimensional alternation of the boundary layer in the wall-perpendicular direction. For a bubble of $d^* < 1$, structural interaction becomes three-dimensional so that Reynolds shear stress of the two-phase mixture decreases. Although the internal flow structure is not measured in the present study, the drag reduction caused by small bubble or microbubble is basically explained by vortex–bubble interaction that restricts the momentum-exchanging events inside the boundary layer but still in deep discussion.

Fig. 12 shows the mean streamwise velocity of bubbles as a function of the bulk mean void fraction. The mean velocity is measured by PIV, i.e. the cross-correlation analysis of bubble image in the flow direction. The ordinate is normalized by the bulk mean velocity of a two-phase mixture U defined by Eq. (3). The vertical bar stands for the standard deviation. The measurement uncertainty of PIV is around 10% in relative error but

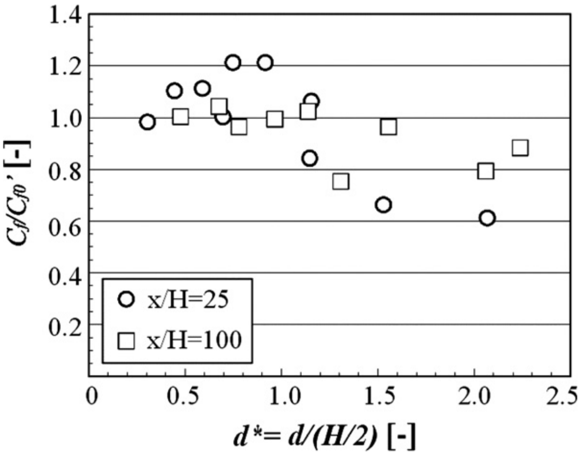

Fig. 11. Bubble size dependency of skin friction in the conditions of $U = 1.0$, 1.5, 2.0 m/s and $x/H = 25$, 100.

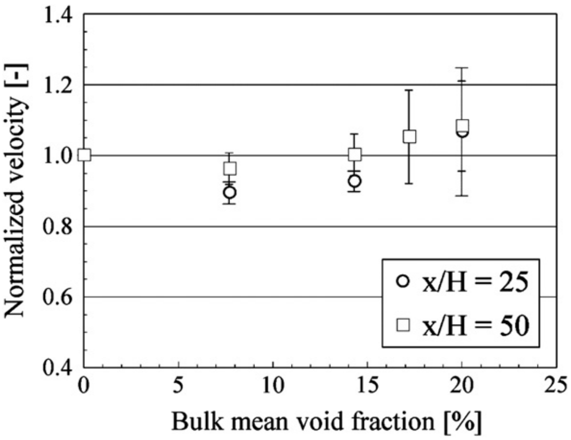

Fig. 12. Mean bubble velocity in streamwise direction vs. bulk mean void fraction at $x/H = 25$ and 50.

that of time average during 50 samples is within 1.5%, much smaller than the deviation of the measurement data. As seen in the figure, the bubbles have a relative velocity to the mixture velocity, up to around 10%. In the case of low void fractions, i.e. small bubbles (see Fig. 10), the bubbles move more slowly than the mixture velocity owing to the fact that the bubbles are suspended near the upper wall where the boundary layer exists. In contrast, the bubbles in large void fractions, i.e. large bubbles, move faster than the mixture velocity. The reason is due to its similarity to a stratified two-phase flow in a channel or tube where the liquid phase experiences friction while the gas phase flows freely. The near-wall local relative velocity between the two-phases was not measured, however, the general trend for the change in void fraction may be similar to the one shown here. Anyhow, the near-wall structure can be discussed in more detail by the quantitative relationship between the local instantaneous skin friction and bubble behaviour. Here the projection void fraction is defined to represent how much bubbles exist near the wall. It is defined by the ratio of a bubble's area to an interrogation area, and measured from the images taken via the high-speed photography.

Fig. 13 shows a typical example of image processing for measuring the local projection void fraction. The raw image (a) is converted to an edge-enhanced image and binarized using an adequate threshold value so as to obtain a bubble image such as (b). The local projection void fraction is calculated in a circular interrogation area the size of which is the same as that of the sensing area of the shear transducer.

3.3. Results of synchronized measurement

Fig. 14 shows the temporal waveforms of the local wall-shear stress (thick line) and the local projection void fraction (thin line). This example is for a bulk mean velocity of 1.0 m/s and a bulk mean void fraction in the

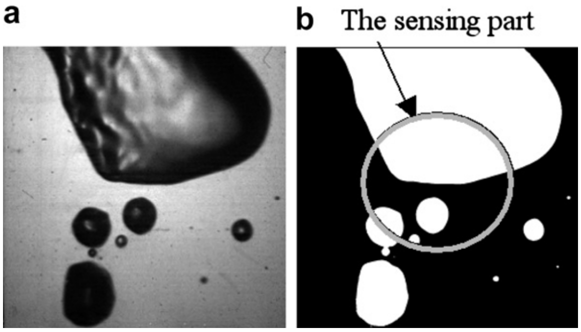

Fig. 13. The definition of projection void fraction. (a) and (b) show the original image and binary image. In (b) the circle indicates the calculating area of the projection void fraction, which is corresponding to the sensing part of the shear transducer.

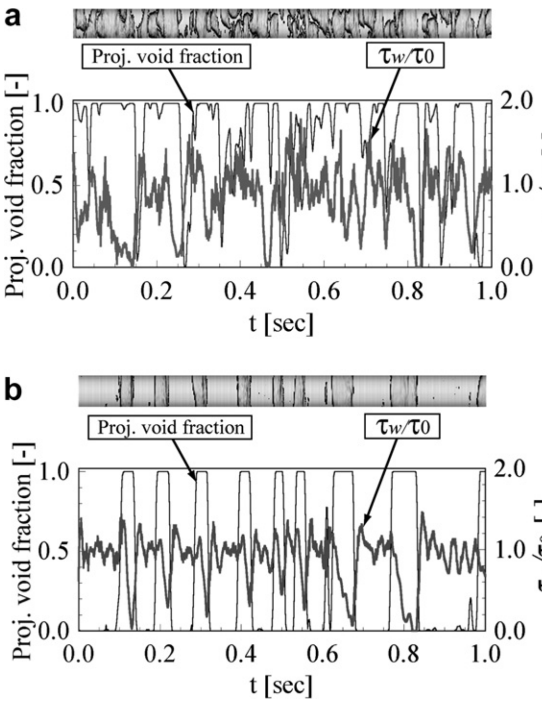

Fig. 14. Correlation of wall-shear stress to void fraction: thick lines indicate the wall-shear stress normalized by that of single phase condition, and thin lines the local projection void fraction. (a) and (b) show the cases of $U = 1.0$ m/s, $\alpha = 20\%$, $x/H = 25$, and $U = 1.0$ m/s, $\alpha = 20\%$, $x/H = 100$.

channel of 20%. The measurement positions are (a) $x/H = 25$ and (b) $x/H = 100$ downstream from the air injection device. In those cases, approximately 30% drag reduction is obtained as the time averaged value. The wall-shear stress in the figure is normalized by that of single-phase flow. When the projection void fraction is unity, it means that a large bubble occupies the interrogation area. The images above the graph are corresponding blow-up images in the time direction during one second. Generally it is clear with the synchronized measurement that there is a negative correlation between the local skin friction and the local void fraction. That is, the skin friction is reduced as bubbles pass the measurement position. In particular, a new finding is that the skin friction decreases drastically in the rear part of an individual bubble. This characteristic becomes more apparent at the downstream position at $x/H = 100$ (see figure b). This trend implies that there is a transient development of the boundary layer of wall-clinging liquid above an individual bubble. The local liquid flow in the front part of the bubble does not suddenly change but gradually changes toward the rear to calm the velocity gradient. This spatial development becomes clearer at the downstream channel because of the stabilization of bubbles' motion. In contrast, the skin friction increases suddenly after a bubble passes and exceeds the skin friction value of single-phase flow. As regards bubble size, which is expressed by the width of the waveform of the void fraction, we see that a large bubble reduces the skin friction for a long period. This fact directly supports the bubble-size dependency, which was described in Section 3.2.

3.4. Local skin friction profiles for individual bubbles

Here, we discuss the local skin friction profile along individual bubbles in the streamwise direction, by analysing the data set from the synchronized measurements. Fig. 15 shows the relationship between the local skin friction and the dimensionless bubble coordinate. The dimensionless bubble coordinate is defined as the time t divided by the bubble passing period τ. The time t is set at zero on the front interface of an individual bubble to be sampled. The coordinate t/τ corresponds to the streamwise length scale x/λ, where x stands for the distance from the front interface, and λ stands for the streamwise length of a bubble. Thus, the graph shows the

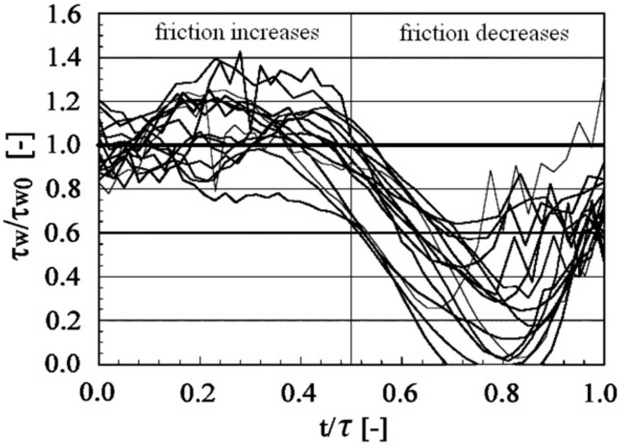

Fig. 15. The relationship between the local skin friction and dimensionless bubble coordinate, denoted by t/τ. t and τ indicate the time at the front edge and the transit time of each bubble.

internal profile of skin friction as a single bubble passes. The bubble front is at the left side of the graph, which is based on a sample of 15 cases ranging in bubble length λ from 20 to 70 mm. The measurement uncertainty for τ is 0.002 s for the typical bubble passing period of 0.1 s; hence the relative error is 2%. With this figure, it is clear that the bubbles have a common profile. That is, the skin friction initially increases in the front part of the bubble but starts to decrease in the middle, and then rapidly falls to reach its minimum value in the rear half. This shows that there is a common spatial development of the liquid shear layer between the wall surface and the bubble's top interface as mentioned before. Namely, the local skin friction modulated by bubbles can be expressed by an invariant function of a single bubble's internal coordinate.

Fig. 16 shows an illustration of a single large bubble migrating to right side with the liquid flow. The bubble shape is quantitatively drawn according to the experimental observation that is viewed in the spanwise direction of the channel. The vertical direction is expanded about 5 times as the real one in the figure for easier understanding of the wall-perpendicular structure. As we imagine from the figure, there is a thin liquid film between the wall surface and the top interface of bubble. The liquid film thickness gradually becomes thinner from the front to the rear part of the bubble so that the skin friction varies along the coordinate. It is known by the paper of Tisne et al. (2003), that the thinner the film becomes, the lower shear stress the film has. This knowledge is consistent to the present profile of the skin friction. The region near the rear edge involves a capillary wave that is confirmed by top-view photographs, as shown in Fig. 9. After the wave, there may

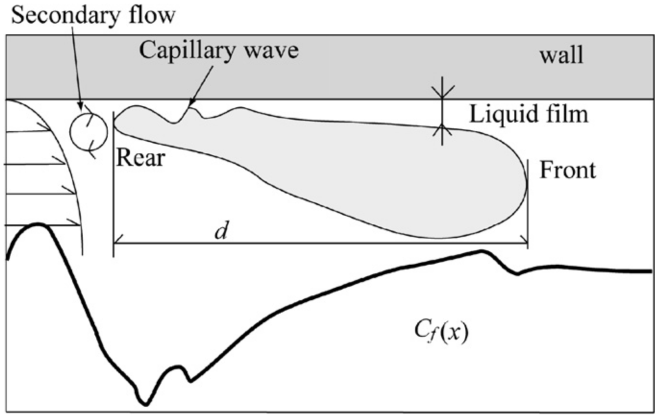

Fig. 16. Flow field around a single large bubble – illustration from the experimental results.

be secondary flow that is generated to connect with the main flow and recover the velocity gradient in the downstream region of the bubble. In this recovery region, the skin friction takes locally high value. In the case of small bubble in the streamwise direction, the drag-reducing effect along the liquid film is shortened but the drag-increasing effect around the rear interface remains so that the average friction increases.

Fig. 17 shows the relationship between the mean skin friction inside a single bubble and its streamwise bubble length. The mean skin friction decreases monotonically with increasing bubble length except for dimensionless bubble lengths of $\lambda/H < 1$. This means that the skin friction reduction in the rear half of individual bubbles persists longest in the case of large bubbles.

Fig. 18 shows the local minimum skin friction detected inside the individual bubble as a function of the bubble length. In comparison with Fig. 17, the minimum skin friction decreases more rapidly as the bubble length increases. When the bubble length becomes longer than 50 mm ($\lambda = 5H$), the local minimum skin friction reaches a value of almost zero. Such a phenomenon is quite similar to air film-based drag reduction, i.e. there is a shear-free structure inside the bubble. In other words, there is a critical bubble length at which bubble-based drag reduction undergoes a transition to air film-based drag reduction.

Fig. 19 shows another type of expression of the local skin friction behaviour inside a single bubble. The ordinate is the same as in Fig. 15 but the abscissa represents the local projection void fraction. These two values are functions of time, and hence the one set of time-series data produces a two-dimensional closed curve. Here the local projection void fraction is low-pass filtered to present a smooth trajectory on the map. The dashed curve indicates the data at the front part of the bubble, at which the temporal derivative of the void fraction is obtained as a positive value. The solid curve indicates that in the rear part. The trajectories clearly show a hysteresis effect in the skin friction, i.e. the local skin friction is not influenced only by the local void fraction. This is a different situation from that in air film drag reduction. This asymmetric feature in the streamwise direction derives from the spatial evolution of the liquid layer that exists between the bubble and the wall surface. To be consistent with the measured friction, the liquid layer must be thinning and decelerating in the rear part of the bubble. One piece of evidence to support this is the fact that a steady capillary wave emerges only in the rear half of the bubble, as shown before.

In our future studies, there are two tasks to be undertaken. One is to develop a tool for predicting the drag reduction effect from bubble size distribution, since it is this that governs the local and average skin friction on

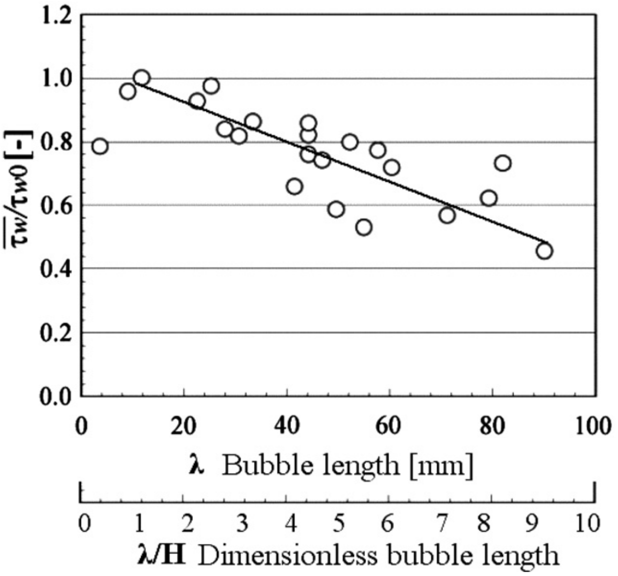

Fig. 17. Mean ratio of wall-shear stress vs. bubble length at $U = 1.0$ m/s, $\alpha = 20\%$, $x/H = 100$: The bubble length λ is estimated by bubbles' streamwise advection velocity U multiplied by bubble's transit time τ. The solid line indicates linearly approximated tendency of the wall-shear stress reduction.

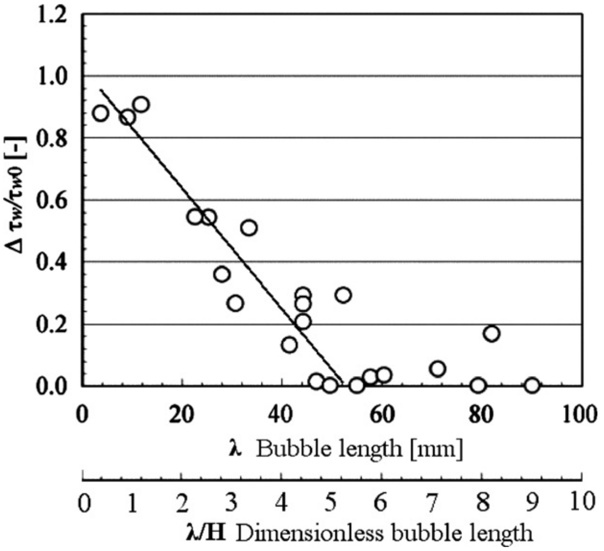

Fig. 18. The variation of ratio of wall-shear stress vs. bubble length at $U = 1.0$ m/s, $\alpha = 20\%$, $x/H = 100$. The solid line indicates linearly approximated tendency which reach zero at $\lambda = 50$ mm or $\lambda/H = 5$.

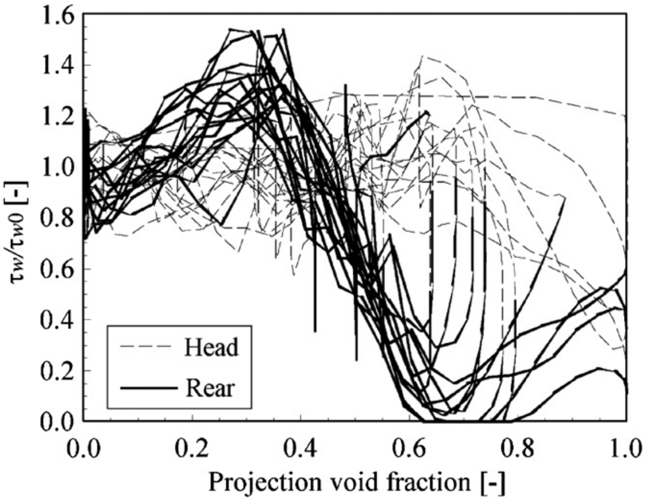

Fig. 19. Hysteresis of wall-shear stress respect to local projection void fraction: $U = 1.0$ m/s, $\alpha = 20\%$, $x/H = 100$.

the target wall as we have shown in this paper. The other is to analyse or measure directly the skin friction reduction process caused by individual bubbles.

4. Conclusions

Skin frictional drag reduction by the use bubbles that are large relative to the shear layer is investigated experimentally using a horizontal rectangular turbulent channel. The present report focuses on the intermediate bubble size condition between those of the microbubble and air film methods. The tested ranges for Weber number and Froude number are chosen such that the bubbles' deformability and buoyant effect play major roles in the alternation process of the boundary layer. Firstly, parametric studies changing the void fraction and the flow speed are presented. Secondly, the temporal relationship between the local skin friction and the bubble interfacial structure is investigated through synchronized measurements. The following conclusions have been obtained.

(1) Skin friction decreases independently on the flow speed when bubbles enough larger than the thickness of the boundary layer are mixed inside the channel. This trend is kept for a long distance up to $x/H = 400$ from the position of bubble generator if void fraction is supplied more than 20%. The gain factor (drag reduction ratio to void fraction) in such a case converges to a constant larger than unity, implying an effective alternation of the boundary layer made possible by the accumulation of large bubbles into the target wall.
(2) Skin friction increases to a maximum as bubble size relative to channel half height approximates to unity. The data reinforce the discovery that avoiding such a bubble condition is essential for bringing about drag reduction. In the upstream region at $x/H = 25$, the skin friction actually increases dependently on the flow speed because of two reasons. One is change in the average bubble diameter with the flow speed, and the other is the two-phase boundary layer that is still in transient state to develop at the position.
(3) It is confirmed with the synchronized measurement that there is a clear negative correlation observed between the local skin friction and the local void fraction. In particular, friction decreases drastically in the rear part of an individual bubble while the front part exhibits a slight increase. This asymmetric profile of the local skin friction is one of the features that are different from the basic idea of the air film method.
(4) The local minimum skin friction inside a single bubble achieves zero if the bubble's streamwise length becomes larger than a critical value. The critical bubble length in the present experiment is $5H$ (H: the channel height). Above the critical value, a locally shear-free structure exists inside the single bubble similarly to that in air film drag reduction.

Acknowledgements

The authors of this paper are grateful for the support of the Office of Naval Research under grant N00014-03-1-0299, to Dr. L. Patrick Purtell, and also to the National Maritime Research Institute of Japan. In addition, a part of the study is supported by Grant-aided scientific research of the Japanese Ministry of Education and Science (MEXT): No. 17686014.

References

Felton, K., Loth, E., 2002. Diffusion of spherical bubbles in a turbulent boundary layer. Int. J. Multiphas. Flow 28, 69–92.
Ferrante, A., Elghobashi, S., 2004. On the physical mechanism of drag reduction in a spatially developing turbulent boundary layer laden with microbubbles. J. Fluid Mech. 503, 345–355.
Fukuda, K., Tokunaga, J., Nobunaga, T., Nakatani, T., Iwasaki, T., 2000. Frictional drag reduction with air lubricant over a super-water-repellent surface. J. Marine Sci. Tech. 5, 123–130.
Gabillet, C., Colin, C., Fabre, J., 2002. Experimental study of bubble injection in a turbulent boundary layer. Int. J. Multiphas. Flow 28, 553–578.
Kato, H., Iwashina, T., Miyanaga, M., Yamaguchi, H., 1999. Effect of microbubbles on the structure of turbulence in a turbulent boundary layer. J. Marine Sci. Tech. 4, 115–162.
Katsui, T., Okamoto, Y., Kasahara, Y., Shimoyama, N., Iwasaki, Y., Soejima, S., Hirayama, A., 2003. A study of air lubrication method to reduce frictional resistance of ship. J. Kansai Soc. N.A., Jpn. 239, 45–53, in Japanese.
Kitagawa, A., Hishida, K., Kodama, Y., 2005. Flow structure of microbubble-laden turbulent channel flow measured by PIV combined with the shadow image technique. Exp. Fluids 38, 466–475.
Kodama, Y., Kakugawa, A., Takahashi, T., Kawashima, H., 2000. Experimental study on microbubbles and their applicability to ships for skin friction reduction. Int. J. Heat Fluid Flow 21, 582–588.
Latorre, R., Miller, A., Philips, R., 2003. Micro-bubble resistance reduction on a model SES catamaran. Ocean Eng. 30, 2297–2309.
Legner, H.H., 1984. Simple model for gas bubble drag reduction. Phys. Fluids 27, 2788–2790.
Madavan, N.K., Deutsch, S., Merkle, C.L., 1985. Measurements of local skin friction in microbubble-modified turbulent boundary layer. J. Fluid Mech. 156, 237–256.
Marie, J.L., 1987. A simple analytical formulation for microbubble drag reduction. J. Phys-Chem. Hydro. 13, 213–220.

Matsumura, K., Kaminaga, F., Saito, H., 2002. Drag reduction on super water repellent surface with air injection method: second report, drag reduction mechanism. Trans. JSME, Ser. B 68, 32–38, in Japanese.

McCormick, M., Bhattacharyya, R., 1973. Drag reduction of a submersible hull by electrolysis. Nav. Eng. J. 85, 11–16.

Merkle, C.L., Deutsch, S., 1992. Microbubble drag reduction in liquid turbulent boundary layers. ASME Appl. Mech. Rev. 45, 103–127.

Moriguchi, Y., Kato, H., 2002. Influence of microbubble diameter and distribution on frictional resistance reduction. J. Marine Sci. Tech. 7, 79–85.

Murai, Y., Oishi, Y., Takeda, Y., Yamamoto, F., 2006. Turbulent shear stress profiles in a bubbly channel flow assessed by particle tracking velocimetry. Exp. Fluids 41, 343–352.

Takahashi, T., Kakugawa, A., Makino, M., Kodama, Y., 2003. Experimental study on scale effect of drag reduction by microbubbles using very large flat plate ships. J. Kansai Soc. N.A., Jpn. 239, 11–20.

Tisne, P., Aloui, F., Doubliez, L., 2003. Analysis of wall shear stress in wet foam flow using the electrochemical method. Int. J. Multiphase Flow 29, 841–854.

Winkel, E.S., Ceccio, S.L., Dowling, D.R., Perlin, M., 2004. Bubble-size distributions produced by wall injection of air into flowing freshwater, saltwater and surfactant solutions. Exp. Fluids 37, 802–810.

Xu, J., Maxey, M.L., Karniadakis, G.E., 2002. Numerical simulation of turbulent drag reduction using micro-bubbles. J. Fluid Mech. 468, 271–281.